Research Article

Amal Y. Aldhebiani, Mohamed Elhag*, and Amjaad A. Alshehri

Consideration of hyperspectral data in intraspecific variation (spectrotaxonomy) in *Prosopis juliflora* (Sw.) DC, Saudi Arabia

https://doi.org/10.1515/geo-2020-0231
received September 10, 2020; accepted January 29, 2021

Abstract: Classification is the science that arranges organisms in groups according to their similarities and differences. In plant science, there are many aspects of classifications. For instance, there is morphological, anatomical, palynological, molecular, and chemical classification. All these types consume time, effort, and money. In this research, new technology is tested to identify the differences between plants. Spectroradiometer will help in classifying *Prosopis juliflora* (Sw.) DC in Bahrah region in Saudi Arabia. Spectroradiometer technology is applied to a sample of 40 taxa of *P. juliflora* in two different seasons. Within each sample site, measurements were taken at a high sun angle from 10:00 am to 2:00 pm. Results showed that spectroradiometer indicated the existence of significant differences among *P. juliflora* taxa. Correspondingly, the spectroradiometer engenders the spectral responses of the targeted species in the region between 400 and 2,500 nm wavelength. The spectral behavior of *P. juliflora* in four seasons was demonstrated as season dependent. The variance-based principal component analysis divided the investigated samples into two groups, either positively correlated or negatively correlated according to the seasonal data collection. Sample number 5 in the quantile's slicing analysis maintained a stable behavior when it was exposed to 100% wavelength. *P. juliflora* behavior was stabilized in the infrared (IR) samples (4,5), the shortwave IR (SWIR) (3,4,5), and thermal IT (TIR) (3,4,5,6) at the quantile range of >75. While in the quantile range <25, we found the stability behavior in the IR samples (2,8,10), the SWIR (2,7,8,10), and in TIR (2,7,8,10). Therefore, this approved that the spectroradiometer is useful as the first classification process. More studies are needed to support this finding, such as chemical and molecular investigations.

Keywords: arid environments, overlapped taxa, phenology, *Prosopis juliflora*, spectral classification, spectroradiometer

1 Introduction

Remote sensing plays a role in understanding these phenomena. Remote sensing gives a lot of information about plants, and the definition illustrates the finding or measuring plant physical, biological, biochemical, or phonological attributes that denote a plant's functional acclimatization, which otherwise reveal the underlying plant ecophysiological processes [1,2]. Other numerous features are pertinent to any discussion of identifying vegetation function with remote sensing, including spatial, spectral, temporal, and biological scopes.

Imaging spectrometers (instruments that gather hyperspectral data) breakdown the electromagnetic spectrum into sets of bands that categorize objects through their spectral properties on the surface of the earth. Hyperspectral data consist of various bands, approximately hundreds of bands, which also include the electromagnetic spectrum [3–5]. Hyperspectral remote sensing, also referred to as imaging spectroscopy, is recently investigated by researchers and professionals to find and identify the terrestrial flora [6–8]. Several ecological applications can benefit from hyperspectral remote sensing, for instance, measuring chlorophyll, leaf water, cellulose, pigments, lignin along with other uses in agriculture, astronomy, chemical imaging, remote sensing [9–11].

* **Corresponding author: Mohamed Elhag,** Department of Hydrology and Water Resources Management, Faculty of Meteorology, Environment and Arid Land Agriculture, King Abdulaziz University, Jeddah 21589, Saudi Arabia; Institute of Remote Sensing and Digital Earth (RADI), Chinese Academy of Science (CAS), Beijing 100094, China; Department of Applied Geosciences, Faculty of Science, German University of Technology in Oman, Muscat 1816, Oman, e-mail: melhag@kau.edu.sa
Amal Y. Aldhebiani, Amjaad A. Alshehri: Biological Sciences Department, Faculty of Science, King Abdulaziz University, Jeddah 21589, Saudi Arabia

Components of biodiversity, which are widely varied in vegetations cover form related biological systems in the Saudi Arabia welfare structure. Studies have indicated contrasts in plants of one physical category because of the distinction of substance and physical properties inside the plant [12,13]. The vegetation structure gave a few contrasts in its spreading conduct in various places in the Kingdom, which can be related to climatic condition changes, water sources, and anthropogenic weights along the rising slope, as reported by Hegazy et al. [14].

Hyperspectral remote sensing applications were continuously developed over the past four decades to add more insights into the natural vegetation behaviors and agricultural practices [15]. Recently, significant scholarly works describe in detail the concept of the ground-based and handheld remote sensing platforms that improved natural vegetation mapping [16–20]. Moreover, data dimensionality and data redundancy are not limiting factors in using hyperspectral data as it was before which led to swift enhancements in hyperspectral remote sensing applications [21,22]. Band selection in hyperspectral data mining is an essential prerequisite to optimize data efficiency and reduce the computational timing [23,24].

Several publications had discussed the hyperspectral sensors on different platforms and their applications. Specifically, handheld spectroradiometers such as analytical spectral devices (ASD) were used extensively in natural vegetation mapping, among other several applications [18,25,26]. ASD spectroradiometers operate generally from 400 to 2,500 nm in a very narrow range of 1 nm bandwidth interval (high-resolution ASD) up to 100 nm bandwidth intervals (low-resolution ASD). Detailed and accurate mapping of natural vegetation and plant taxonomical models was achieved using the thermal infrared (TIR) spectrum [27,28]. The new generation of the hyperspectral sensors such as spatially enhanced broadband array spectrograph system will expand the resources and the interpretation of the hyperspectral remote sensing data [29,30].

In line with Alfarhan [31] and Thomas et al. [32], vegetation species in Saudi Arabia are divided into three general categories, namely, species of the Sudano–Deccanian zone, Saharo–Sindian zone, and Tropical Indian–African categories. The annual average rainfall in the northwestern regions of Saudi Arabia differs from 30 mm in the northern areas to 90 mm in the northeast. Rainfall records in the central region of the Kingdom, mainly in the Riyadh region, indicate that rainfall is increasing from South to North and from East to west, ranging between 100 and 85 mm annually. Generally, the annual average rainfall is less than 100 mm and most of it is in December, January, February, and March and considerably helps for the growth of short-lived vegetation.

Many scholarly works had been published on the flora of Saudi Arabia. According to El-Sheikh and Yousef [33], Mandaville and Mandaville [34], and Thomas et al. [35], the most comprehensive works are two flora books: the first is Flora of Saudi Arabia written by Migahid et al. [36] and published four times. The second is the Flora of the Kingdom of Saudi Arabia written by Chaudhary [37]. Several studies were conducted in different regions of Saudi Arabia such as Batanouny [38] and Aldhebiani et al. [39] who studied the vegetation and floras of the sabkhas, hillocks, and other prominent mountains of the Najd region, such as Tuwaiq, Aja, and Salma. Considerable efforts have also been made toward the elucidation of vegetation–environmental relationships in the ecosystems "raudhas" or depressions [40–42]. The plant communities of Wadis have been addressed in some studies such as Wadi Al-Ammaria [43] and Wadi Hanifa [44]. The *Prosopis juliflora* species, in the Kingdom of Saudi Arabia, is endangered due to their limited genetic range and geographical variety, minor population size, short density, threatening ecological conditions, and unselective tree cutting, regardless of the truth that these species have a great reproductive ability [45–47].

In the study area considered in this research, Bahrah, west of Saudi Arabia, no studies have been endeavored to classify *P. juliflora* species using different wavelengths. The current study addressed the consideration of hyperspectral data in intraspecific variation in *P. juliflora* (Sw.) DC, Saudi Arabia, to identify the significance of different responses of the *P. juliflora* taxa to different spectral wavelengths such as visible spectrum, short-wavelength IR, long-wavelength IR, and TIR. The study goal is to investigate the impact of different wavelengths on different leaf samples collected from different *P. juliflora* taxa to study their spectral signature behavior and to appraise the impact of these different wavelengths on these species' occurrence.

2 Materials and methods

2.1 Study area description

The climate of Saudi Arabia is classified as an "arid climate" within Thornthwaite's global climatic classification, and as "dry climates" in Koppen's classification [48,49].

According to Juneidi and Huss [50], relative humidity is normally low excluding the coastal areas, where it touches above 90%. The annual average temperature is virtually 33.4 and 14°C in summer and winter, respectively. Hot weather describes the Kingdom's climate for the larger part of the year. The north winds move from the eastern Mediterranean in the direction of the Arabian Gulf with some extensive variations [51]. Spectral data are gathered in the Bahrah region, 21.392245°N, and 39.472352°E. Bahrah is located on Tihama plateau closer to Wadi Fatima between Jeddah and Makkah (Figure 1). The climate in Bahrah Dafi is mild in summer and rainy in winter. The average summer temperature is reported as 33°C and the average rainfall is 520 mm. The greatest amount of rainfall is in January and the lowest amount is in July [52]. Inside the study region, different sites have been chosen as samples in an exploration tour preceding the beginning of the arena campaign for the gathering of spectral data. The arena campaign commonly has a multitemporal framework, gathering spectra from diverse sorts of plants at diverse phenological periods and different periods of the year [39].

2.2 Field sampling

The spectroradiometer is plugged into the Ethernet cable and ends with a pistol to measure the spectrum and wave oriented. The Spectralon® White Reference panel [53] is installed for utilization and handling of the diverse segments, and the panel is in black to decrease the scattering of the related radiance (Figure 2).

The leaves of *P. juliflora* were cut from several trees in different seasons where the tree is about 2 m long. More than 40 samples in every sample site were calculated at a high sun angle, from 10 am to 2 pm by spectroradiometer technology. The following are the fundamental steps followed in undertaking two experiments on *P. juliflora* species:

(1) *P. juliflora* leaves were collected from 10 trees of which two samples were taken at different seasons.
(2) Other samples were collected from the plant to chemically measure them in addition to the soil.
(3) Leaves of the plant were weighed in the wet content and then dried. After drying, the leaves were weighed in dry wax to determine the water content.
(4) Dry leaves were measured by spectroradiometer, and data collected from the files of spectral data were

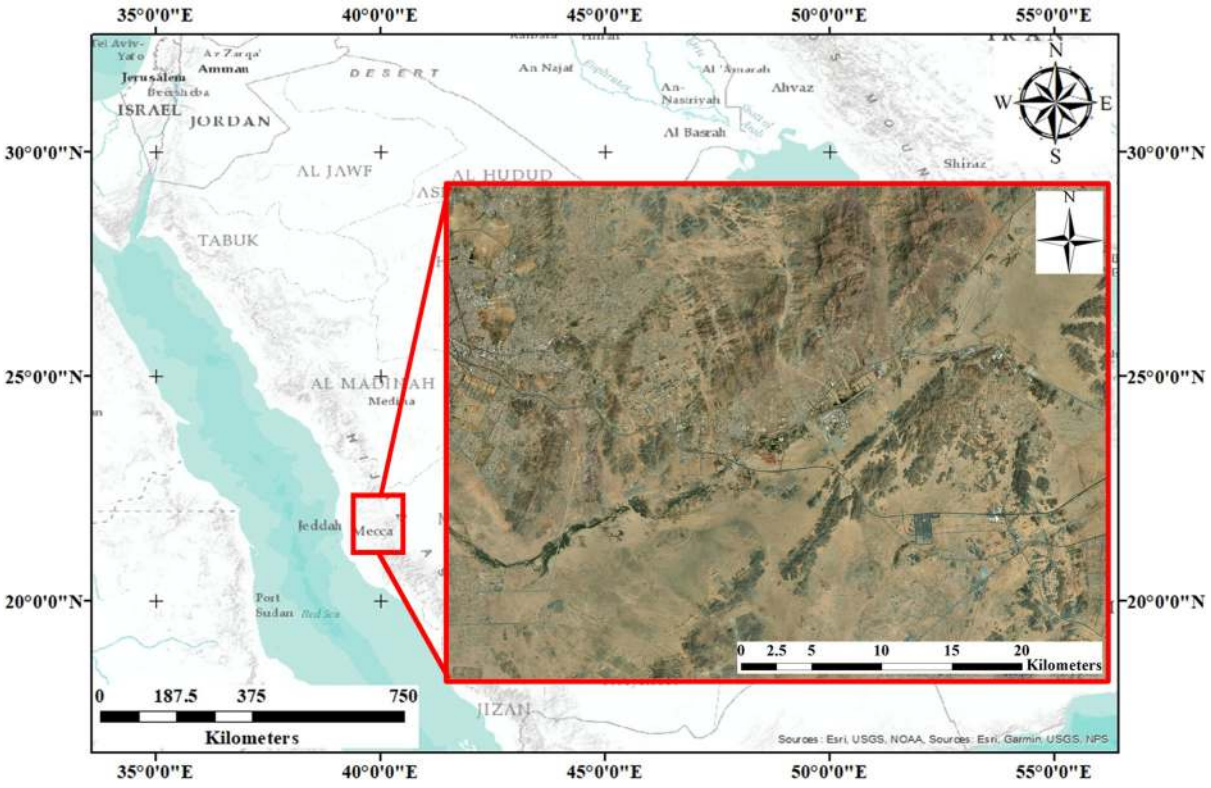

Figure 1: The location of the study area sampling site disclosed Bahrah area.

Figure 2: Pictures showing the mechanism of work (1) plant leaves, (2) black plate, (3) spectroscopy, (4) white reflector, (5) measured by pistol, and (6) transfer of data to the laptop.

transferred as a format of ASCII text by applying the software of ASD ViewSpec Pro.

2.3 Hyperspectral data processing

Spectral varieties with extreme noise at the final point of the spectrum, from 2,350 to 2,500 nm, and with obvious robust climatic intervention, that is 1,351–1,449 nm and 1,801–2,029 nm, were discarded from the investigation. Accordingly, the spectral data were modified for steps, i.e., sudden alterations of the noted reflectance that took place in the spectral signatures at 1,000 nm, which is typical for the instrument utilized, as a result of the instrument sensitivity drift. The shortwave IR (SWIR) portion of the spectrum, ranging from 1,000 to 1,800 nm, was considered as a corrections' reference since it is constant to the instrument's sensitivity drift [54,55]. To conclude, the spectral data are saved with the auxiliary metadata in a uniform, accessible to track method [56].

Figure 3 shows the behavior of the natural vegetation to different electromagnetic wavelengths. For the visible spectrum, that is, from 1 to 395, the plant taxa do not reveal any significant difference. For the long-wavelength IR, that is from 442 to 1,079, the taxa reveal a significant difference among the species. In its response to the SWIR,

that is, from 1,128 to 1,569, the plant taxa reveal only one sample differs from others. For the TIR, that is, from 1,618 to 2,108, the trees reveal that two of the samples are similar in their behavior to the TIR and one sample differs from them in its response to the TIR wavelength.

2.4 Principal component analysis (PCA)

The PCA is used to transform a set of likely correlated to unlikely correlated variables. The principal component number is less than or equal to the variables' original number. According to Lorenz [57] and Jolliffe and Cadima [58], the PCA's fundamental equations are described as follows:

$$w_{(1)} = \arg \max_{\|w\|=1} \left\{ \sum_i (t_1)_{(i)}^2 \right\} = \arg \max_{\|w\|=1} \left\{ \sum_i ((x_{(i)}) \cdot w)^2 \right\} \quad (1)$$

To maximize variance, the first weight vector $w_{(1)}$ thus has to be satisfied equivalently, and writing this in matrix form gives

$$w_{(1)} = \arg \max_{\|w\|=1} \{\|Xw\|^2\} = \arg \max_{\|w\|=1} \{w^{\mathrm{T}} X^{\mathrm{T}} X w\} \quad (2)$$

Since $w_{(1)}$ has been defined to be a unit vector, it also equivalently satisfies to be calculated as follows:

$$w_{(1)} = \arg \max \left\{ \frac{w^{\mathrm{T}} X^{\mathrm{T}} X w}{w^{\mathrm{T}} w} \right\} \quad (3)$$

The Kaplan–Meier estimator, also known as the product-limit estimator, is a nonparametric statistic used to estimate the survival function from lifetime data, survival estimates, exploratory plots with optional parameter estimates, and a comparison of survival curves when there is more than one group, using designated sample data table [59,60]. The summary report gives estimates for the mean survival time as follows:

$$\hat{S}(t) = \prod_{i:\ t_i \le t} \left(1 - \frac{d_i}{n_i}\right) \quad (4)$$

With t_i is the time when at least one event happened, d_i the number of events that happened at time t_i, and n_i the individuals known to have survived (have not yet had an event or been censored) up to time t_i.

2.5 Statistical functions

Quantile analysis is a binary form of spectral data classification, which Khan et al. [61] used to improve the algorithm performance as a functional gradient descent (FGD). The generic form of the FGD is valid to analyze high spectral data precisely throughout a direct data interpretation.

$$Q_\tau(Y) = \arg \min_c E_Y[\rho_\tau(Y - c)] \quad (5)$$

Where

$Q_\tau(Y)$ is the τth quantile of Y,

$\rho_\tau(r)$ is the conditional function

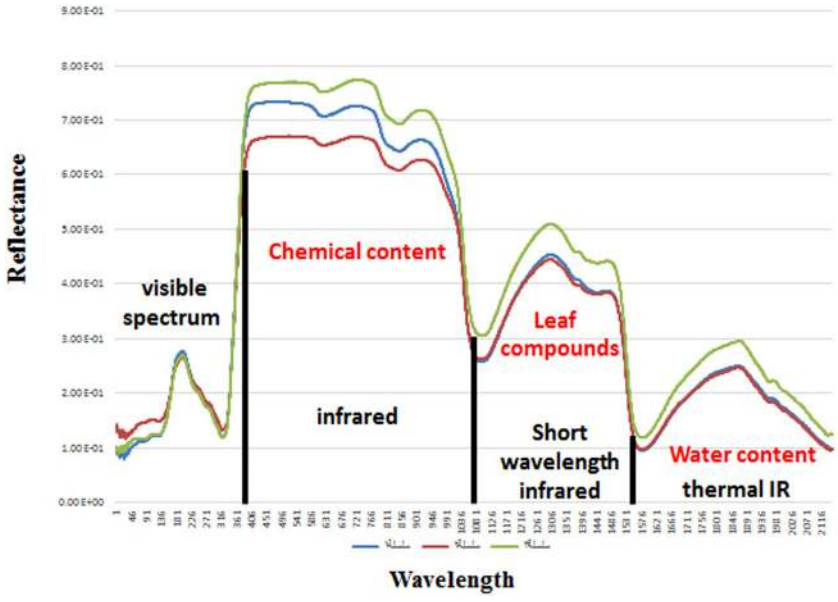

Figure 3: Vegetation behavior subjected to a different spectrum of a different wavelength.

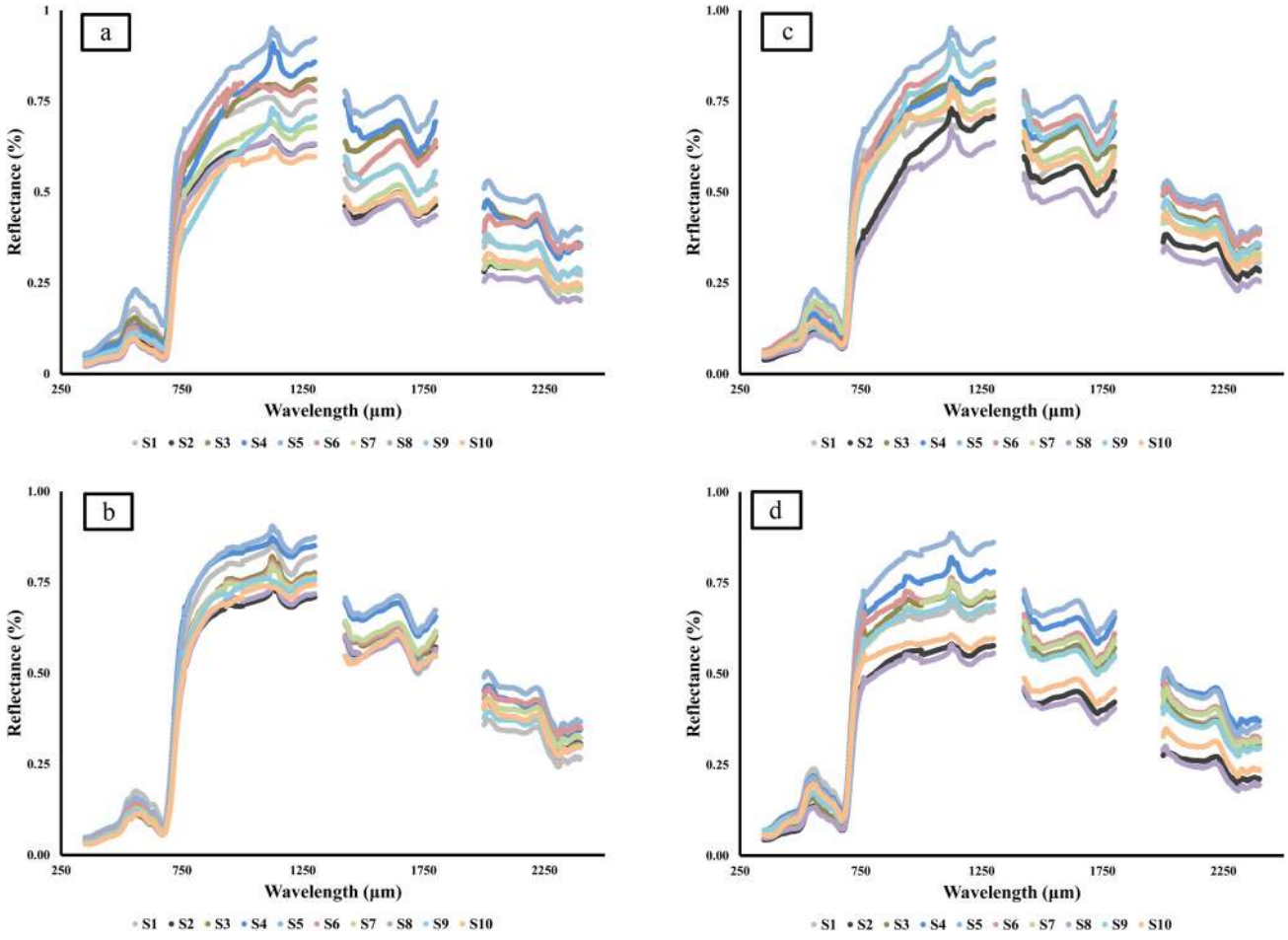

Figure 4: The wavelength vs reflectance of *Prosopis juliflora*, (a) result collected in Feb. 2019, (b) result collected in Sep. 2019, (c) result collected in Nov. 2019, and (d) result collected in Feb. 2020.

While the τth conditional quantile of Y given x be $f(x)$ for a given quantile estimation:

$$\int^{[0]} (.) = \arg\min_c \frac{1}{n} \sum_{i=1}^{n} \iota(Y_i, c) \tag{6}$$

The functions with Col prefix compute statistics for a column of numbers or expressions which specifically includes the mean, quantile, range, maximum, and minimum. The Col quantile functions of Bassett Jr and Koenke [62], represent the quantile percentage divided by 100. The 25% quantile, also called the lower quartile, corresponds to $p = 0.25$, and the 75% quantile, called the upper quartile, corresponds to $p = 0.75$. In general, to define the quantile that corresponds to the fraction p, linear interpolation between the two nearest pi is used. According to Ashkar and Ouarda [63], if p lies as a fraction of f from pi to pi^{+1}, then pth quantile is defined as:

$$Q(p) = (1 - f)\,Q(pi) + fQ(pi^{+1})$$

As special cases, define the median and quartiles by:
Median: Q (5)
Lower quartile: Q (25)
Upper quartile: Q (75)

The function Q defined in this way is called the quantile function.

$$\text{Col Quantile}\left(\text{age}, \frac{(\text{Row}() - 1)}{(\text{NRow}() - 1)}\right) \quad \text{Col Quantile}\left(\text{age}, \frac{(\text{NRow}() - \text{Row}())}{(\text{NRow}() - 1)}\right) \tag{7}$$

3 Results and discussion

In the current study, the ASD spectroradiometer illustrates the different spectral signatures over the visible,

near infra red (NIR), and SWIR spectral bands [64]. Correspondingly, the spectroradiometer engenders the spectral responses of the targeted species in the region between 400 and 2,500 nm wavelength. Figure 4 shows the spectral behavior of *P. juliflora* in four seasons and different periods in terms of wavelength against reflection by ASCII text accompanied by the software of ASD ViewSpec Pro.

The results of the PCA were illustrated in Figure 5. Principally, Figure 5a shows the variance-based PCA of the ten different sample indicators where the analysis was divided into two groups. The first group involves the positive samples of S4–S5–S6–S7–S9, and the negative group involves the samples S1–S2–S3–S8–S10. While Figure 5b shows the variance-based PCA collected in summer. The ten different sample indicators were divided into two groups: the first group involves the positive samples of S1–S5–S4, and the negative group involves the samples S2–S3–S6–S7–S8–S9–S10. Figure 5c shows the variance-based PCA where the ten different sample indicators were also divided into two groups. The first group involves the positive samples of S1–S3–S4–S5–S6, and the negative group involves the samples S2–S7–S8–S9–S10. Finally, Figure 5d shows the variance-based PCA collected in winter 2020, and the ten different sample indicators were divided into two groups according to the correlation coefficient value [65].

Spectral information collected from the vegetative covers is generally indicated as a difference in the molecular character of the designated targets. Divergence data were a gradually changing wavelength function; therefore, it gives data that are not likely interconnected with any spectral calculations carried out in a system [66,67]. The analysis of the hyperspectral image, during the previous decade, had developed into one of the best potent and wildest rising technologies in the area of remote sensing [68,69].

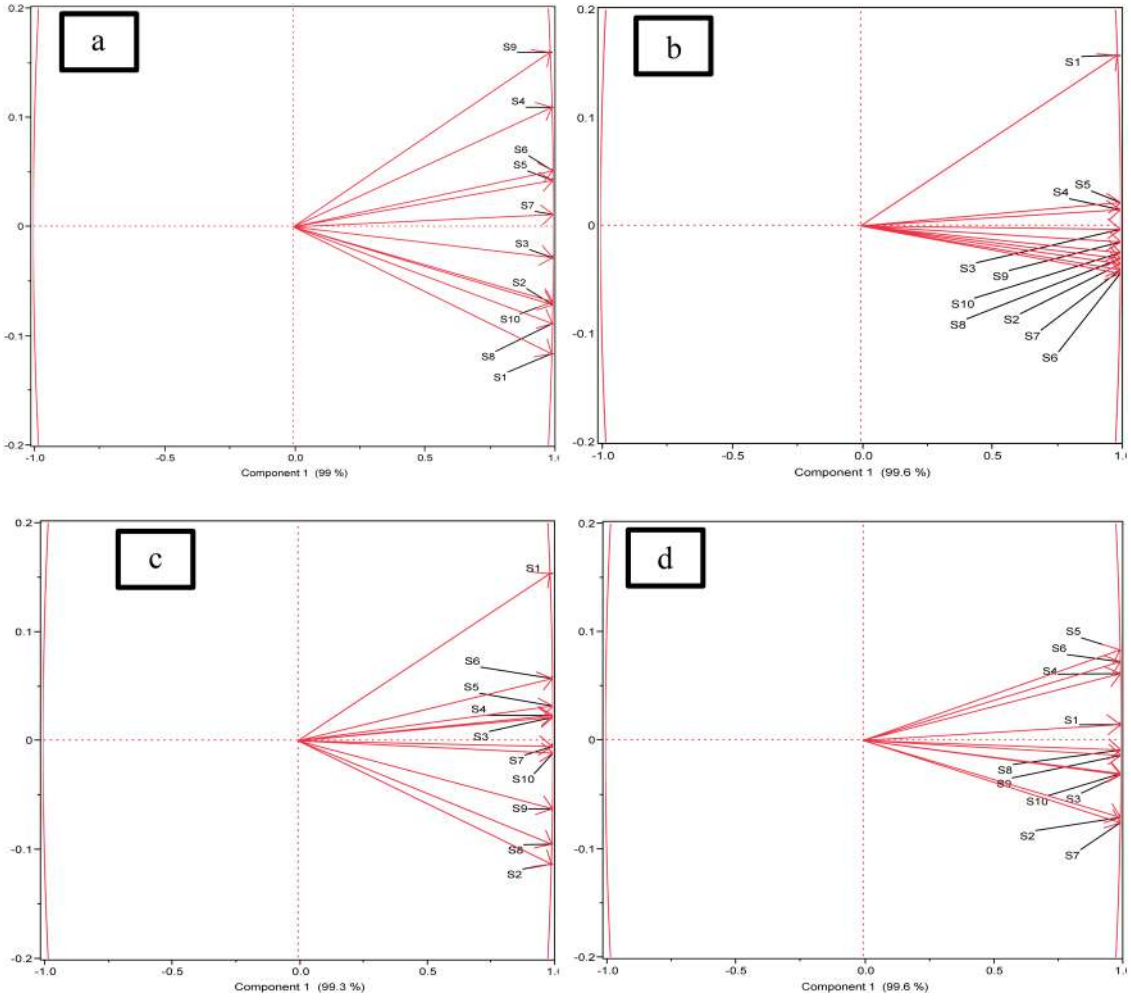

Figure 5: Principal component analysis. (a) Result collected in Feb. 2019, (b) result collected in Sep. 2019, (c) result collected in Nov. 2019, and (d) result collected in Feb. 2020.

Table 1: Quantiles slicing analysis of *Prosopis juliflora*

(**a**) **Result collected in Feb. 2019**

	T1	S1	S2	S3	S4	S5	S6	S7	S8	S9	S10
100.0%	Max	0.75998	0.65156	0.81047	0.90976	0.95114	0.80032	0.69253	0.64990	0.73011	0.62004
99.50%		0.75986	0.64914	0.80926	0.90113	0.94337	0.79788	0.69114	0.64752	0.72403	0.61734
97.50%		0.75751	0.63724	0.80447	0.86081	0.92110	0.79377	0.68352	0.63778	0.70568	0.60085
90.00%		0.74176	0.62384	0.78557	0.82587	0.89004	0.78389	0.66912	0.62448	0.67442	0.59059
75.00%	Quartile	0.68538	0.57103	0.68073	0.69554	0.77031	0.72146	0.59955	0.56141	0.56621	0.53662
50.00%	Median	0.50901	0.43752	0.59829	0.58616	0.68110	0.55920	0.45518	0.41819	0.43792	0.44694
25.00%	Quartile	0.27738	0.23438	0.34390	0.33800	0.39047	0.35005	0.23090	0.20595	0.27646	0.24444
10.00%		0.10298	0.06157	0.09557	0.08594	0.14111	0.06420	0.04543	0.04423	0.07407	0.05090
2.50%		0.05642	0.03849	0.06217	0.06146	0.06687	0.04089	0.02963	0.02855	0.04530	0.03594
0.50%		0.04618	0.03064	0.05156	0.05295	0.05663	0.03183	0.02248	0.02212	0.03889	0.02796
0.00%	Min	0.04553	0.02985	0.05081	0.05233	0.05564	0.03116	0.02163	0.02136	0.03823	0.02685

(**b**) **Result collected in Sep. 2019**

	T2	S1	S2	S3	S4	S5	S6	S7	S8	S9	S10
100.0%	Max	0.85986	0.74088	0.82104	0.87244	0.90438	0.80695	0.79689	0.75318	0.76183	0.74386
99.50%		0.85618	0.73629	0.81603	0.87002	0.90112	0.80318	0.79209	0.74861	0.76152	0.74307
97.50%		0.83777	0.71558	0.79027	0.85714	0.88149	0.77987	0.77022	0.72552	0.75886	0.73995
90.00%		0.81402	0.69792	0.76500	0.84262	0.86035	0.75707	0.75066	0.70841	0.74938	0.73010
75.00%	Quartile	0.76526	0.65510	0.70466	0.80040	0.80343	0.70779	0.70554	0.66460	0.69998	0.67204
50.00%	Median	0.53300	0.53123	0.55533	0.62498	0.63333	0.56750	0.57015	0.52076	0.53018	0.52696
25.00%	Quartile	0.26287	0.29614	0.29430	0.33539	0.36001	0.34301	0.31755	0.28662	0.29306	0.29006
10.00%		0.09844	0.07719	0.06424	0.08227	0.09017	0.07800	0.07326	0.06695	0.06972	0.06493
2.50%		0.04116	0.04605	0.04242	0.05441	0.05710	0.04742	0.04468	0.04469	0.04062	0.03314
0.50%		0.03790	0.03979	0.03490	0.04422	0.04892	0.03970	0.03770	0.03614	0.03420	0.03029
0.00%	Min	0.03778	0.03934	0.03376	0.04273	0.04826	0.03862	0.03695	0.03514	0.03365	0.03015

(**c**) **Result collected in Nov. 2019**

	T3	S1	S2	S3	S4	S5	S6	S7	S8	S9	S10
100.0%	Max	0.70374	0.73011	0.81047	0.81435	0.95114	0.90370	0.79675	0.67049	0.90976	0.78604
99.50%		0.70338	0.72403	0.80926	0.81014	0.94337	0.89480	0.78988	0.66374	0.90113	0.77687
97.50%		0.70129	0.70568	0.80447	0.79981	0.92110	0.86173	0.75803	0.63576	0.86081	0.74285
90.00%		0.68940	0.67442	0.78557	0.77506	0.89004	0.82969	0.73032	0.60741	0.82587	0.71325
75.00%	Quartile	0.65968	0.56621	0.68073	0.68779	0.77031	0.72237	0.64245	0.50801	0.69554	0.64945
50.00%	Median	0.52984	0.43792	0.59829	0.61097	0.68110	0.62747	0.55300	0.40682	0.58616	0.54060
25.00%	Quartile	0.30735	0.27646	0.34390	0.38138	0.39047	0.37521	0.32332	0.24635	0.33800	0.30468
10.00%		0.10666	0.07407	0.09557	0.11010	0.14111	0.12386	0.12237	0.07546	0.08594	0.08705
2.50%		0.06388	0.04530	0.06217	0.07043	0.06687	0.07701	0.06541	0.05327	0.06146	0.06216
0.50%		0.05347	0.03889	0.05156	0.05549	0.05663	0.06555	0.05936	0.04695	0.05295	0.05353
0.00%	Min	0.05279	0.03823	0.05081	0.05310	0.05564	0.06495	0.05911	0.04650	0.05233	0.05281

(**d**) **Result collected in Feb. 2020**

	T4	S1	S2	S3	S4	S5	S6	S7	S8	S9	S10
100.0%	Max	0.69234	0.58137	0.75280	0.81979	0.88688	0.76428	0.75530	0.57925	0.71348	0.60727
99.50%		0.69011	0.58013	0.74885	0.81572	0.88415	0.75961	0.75159	0.57562	0.71106	0.60582
97.50%		0.67469	0.57537	0.72466	0.78957	0.86611	0.73158	0.72878	0.55663	0.69281	0.59762
90.00%		0.66113	0.56421	0.70432	0.76716	0.84874	0.71266	0.70832	0.54513	0.67646	0.58834
75.00%	Quartile	0.63442	0.53596	0.65837	0.71827	0.79102	0.68320	0.63876	0.52099	0.64133	0.56869
50.00%	Median	0.53035	0.41207	0.53566	0.61162	0.64247	0.57004	0.54949	0.38933	0.52360	0.44741
25.00%	Quartile	0.29460	0.21123	0.29788	0.37216	0.34893	0.32017	0.31377	0.19212	0.29187	0.23656
10.00%		0.13727	0.07522	0.08810	0.12950	0.12334	0.11725	0.10230	0.07843	0.10932	0.11082
2.50%		0.07223	0.05043	0.06347	0.08409	0.07496	0.07966	0.07260	0.05448	0.07742	0.05723
0.50%		0.06632	0.04378	0.05006	0.07126	0.06707	0.06780	0.06573	0.04855	0.07085	0.05441
0.00%	Min	0.06620	0.04354	0.04908	0.06992	0.06689	0.06697	0.06553	0.04842	0.07060	0.05424

Table 2: Spectral signature stability behavior of *Prosopis juliflora*

	Quantiles range	Infrared	SWIR	Thermal IR	Stability behavior
T1	>75	4,5	3,4,5	3,4,5,6	4,5
	75 > *x* < 25	1,3,6,7,9	1,6,9	1,9	
	<25	2,8,10	2,7,8,10	2,7,8,10	2,8,10
T2	>75	1,4,5	4,5	4,5	4,5
	75 > *x* < 25	3,6,7,9	1,3,6,7	3,6,7,9	
	<25	2,8,10	2,8,9,10	1,2,8,10	2,8,10
T3	>75	4,5,6,9	4,5,6,9	4,5,6	4,5
	75 > *x* < 25	1,3,7	1,3,7	1,3,7,9	
	<25	2,8,10	2,8,10	2,8,10	2,8,10
T4	>75	4,5	4,5	4,5	4,5
	75 > *x* < 25	1,3,6,7,9	1,3,6,7,9	1,3,6,7,9	
	<25	2,8,10	2,8,10	2,8,10	2,8,10

The first group involves the positive samples of S1–S4–S5–S6, and the negative group involves the samples S2–S3–S7–S8–S9–S10. PCA is a statistical process that aims to increase the interpretation of information by using JMP Statistical software.

Classification of different indicators was possible because of PCA, which identifies the similarities and differences in all samples [70]. The abovementioned sample (a–d) represents the grouping to different indices according to PCA on covariance [71,72]. The samples were categorized into two positive and negative groups, but it was not precisely determining the behavior; and to ensure that a quantitative segmentation analysis of the samples was performed for further clarification [2].

Table 1 shows the quantiles' slicing for the four periods (T1, T2, T3, and T4.) where the data was extracted by equations 5–7. The table was divided from 0.00% (min value) to 100% (max value), while the median specifies the 50% of the recorded reflection values. Interpreting the data in the tables maintained the stability behavior of the tested sample when it was exposed to different wavelengths reflecting from 0 to 100%; while between 75 and 25%, the targets had other interpretations that will not be further addressed.

Table 2 shows the spectral signature stability behavior of *P. juliflora* as clarified in the previous tables, since the spectrum behavior was stabilized in (T1) in the IR samples (4,5), the SWIR (3,4,5), and TIR (3,4,5,6) at the quantile range >75. While in the quantile range <25, we found that the stability behavior in the IR samples (2,8,10), the SWIR (2,7,8,10), and in TIR (2,7,8,10).

In (T2) in the IR samples (1,4,5), the SWIR (4,5), and TIR (4,5) were at the quantile range of >75. In the quantile range of <25, the stability behavior in the IR samples was (2,8,10), the SWIR (2,8,9,10), and TIR (1,2,8,10). In (T3) at the quantile range of >75, the IR samples were (4,5,6,9), the SWIR (4,5,6,9), and TIR (4,5,6). In the quantile range of <25, the stability behavior in the IR samples was (2,8,10), the SWIR (2,8,10), and TIR (2,8,10). In (T4) at the quantile range of >75, the IR samples were (4,5), the SWIR (4,5), and TIR (4,5). In the quantile range of <25 the stability behavior in the IR samples was (2,8,10), the SWIR (2,8,10), and TIR (2,8,10).

This explains the significance of the difference in the chemical content, leaf content, or water content. This is confirmed by a study carried out by Hoshino et al. [73] and Vidhya et al. [71], which showed that the NIR reflectance of the *P. juliflora* leaves correlated significantly with a leaf content.

The common factor between wavelengths and reflectances is the stability behavior that was established in two groups: the first group >75, the samples were (4,5), and the second group <25 the samples were (2,8,10). These results confirm that the *P. juliflora*, under different ranges of wavelengths, exhibited different spectral behaviors, although there is a great similarity in the external appearance of the plant. This also confirms that the hyperspectral spectroradiometer is an effective device, as it gave a good result, and, therefore, it can be effectively used in plant classification [74].

The implementation of the FGD algorithm extended to a robust and reliable classification function of two overlapped plant samples. The plant materials under investigation belong to two different classes along the broad spectral wavelengths. The temporal analysis confirms the designation of the two groups (4 and 5, 2 and 8, and 10) which is a solid finding of the current research of *P. juliflora* spectral classification. The classification algorithm was performed based on labeling the class variables and the corresponding class quantiles to attain equality.

This is consolidated by the findings of the study carried by Suleiman et al. [75] which confirmed that the hyperspectral spectroradiometer is an effective device as the wavelength of numerous IR absorption bands is a definite category of chemical bonds in the leaf samples of plants [76,77] (Figures 6 and 7).

4 Conclusions and recommendations

The extended use of remote sensing concepts in the form of hyperspectral data analysis plays an important role

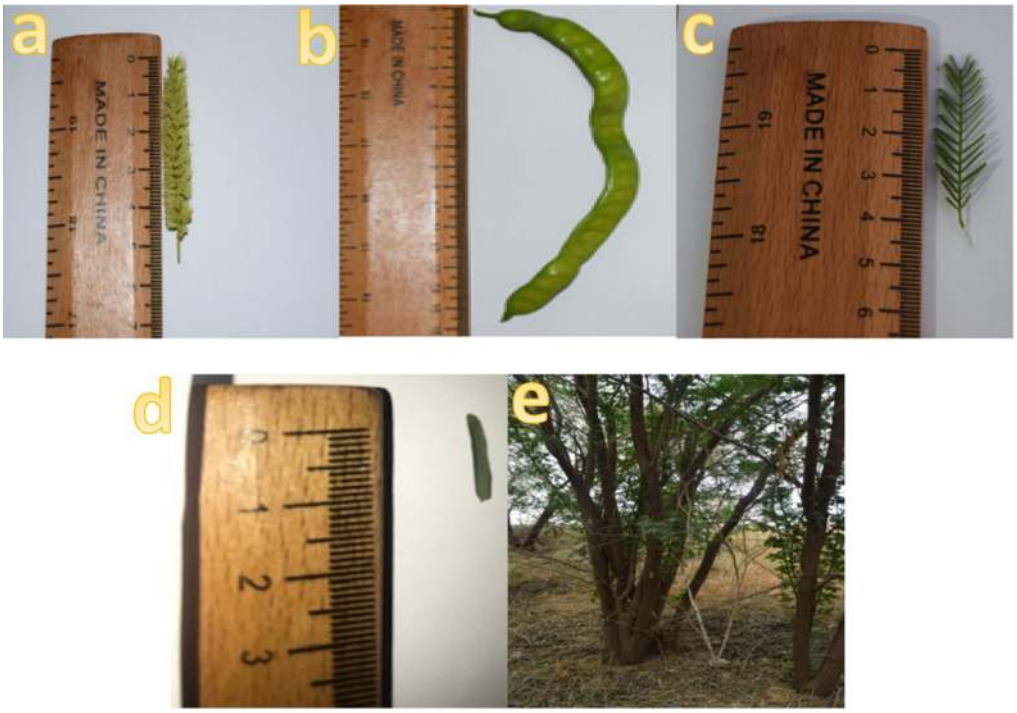

Figure 6: (a) The flower of *Prosopis juliflora* number 10, (b) the fruit (legume), (c) the leaf (compound), (d) the leaflet (compound), and (e) the tree of sample 4.

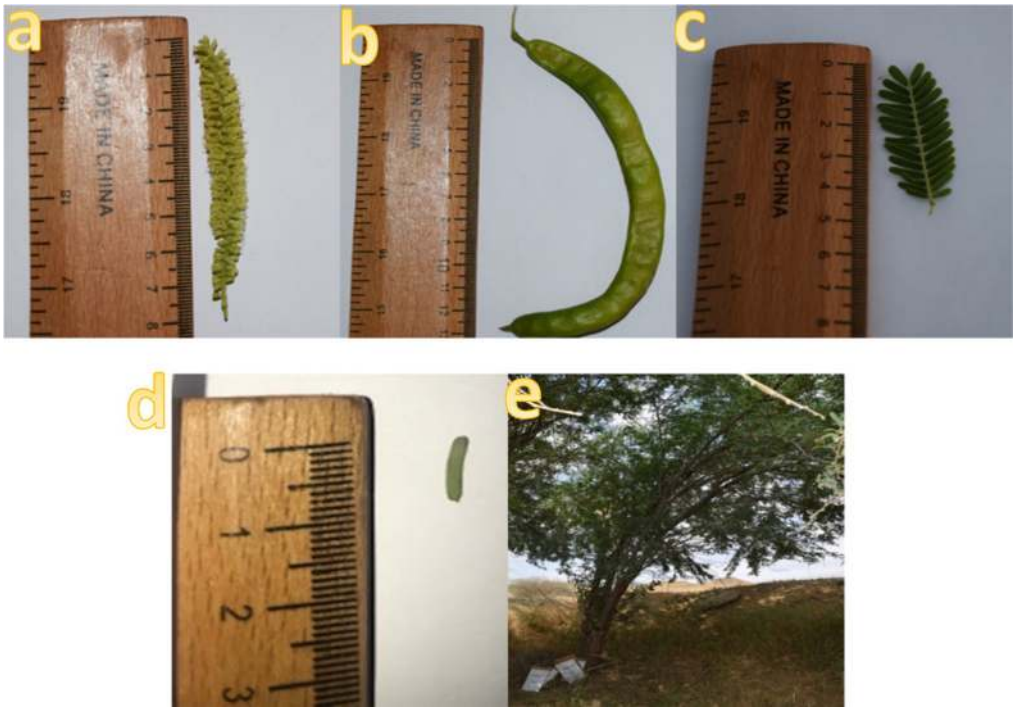

Figure 7: (a) The flower length of *Prosopis juliflora* number 5, (b) the fruit (Legume), (c) the leaf (compound), (d) the leaflet (compound), and (e) the tree of sample 5.

in plant taxonomy. The overlapped plant species are usually distinguished in more complicated gene-level classification to retain their separability. In the current research study, the hyperspectral data of *P. juliflora* collected by temporal screening using the functional gradient decent classification algorithm, which successfully distinguished two separable groups based on the spectral reflectance obtained from different wavelengths.

Prosopis trees play a vital part in the ecology and the economy of many arid and semi-arid zones. They play an integral part in several sustainable lands while preventing further soil degradation and assisting land reclamation use systems that are improving the livelihoods of rural desert populations. Most of the silvicultural constraints to arid zone development have already been overcome, particularly in plantation and establishment nursery, making the most of the best genetic material available, with so many *Prosopis* trees already planted and often spreading widely by natural regeneration.

P. juliflora is one of the rare wood-producing plant species capable of developing in the Arabian Peninsula. The following are some recommendations stated by the researcher in this study. It is the tree best recommended for reclaiming sand dunes in Saudi Arabia in sandy areas. It is a natural source of wood, fuel, and coal. It contributes to regulating bowel movement and helps preventing constipation because it absorbs water, which causes the intestine to normally work. Finally, it is recommended that more research is performed to study about this very important tree, focusing on other aspects such as the medicinal values of the seeds, fruits, flowers, and leaves.

Acknowledgment: This project was funded by the Deanship of Scientific Research (DSR), King Abdulaziz University, Jeddah, under grant no. G-423-247-1440. The authors, therefore, acknowledge with thanks to DSR's technical and financial support.

References

[1] Poorter H, Anten NP, Marcelis LF. Physiological mechanisms in plant growth models: do we need a supra-cellular systems biology approach? Plant Cell Environ. 2013;36:1673–90.
[2] Elhag M. Understanding of photosynthetically active radiation index under soil salinity variation using remote sensing practices in arid environments. Desal Wat Treat. 2018;112:171–8.
[3] Landgrebe D. Hyperspectral image data analysis. IEEE Signal Process Mag. 2002;19:17–28.
[4] Dalponte M, Ørka HO, Gobakken T, Gianelle D, Næsset E. Tree species classification in boreal forests with hyperspectral data. IEEE Trans Geosci Remote Sens. 2012;51:2632–45.
[5] Adão T, Hruška J, Pádua L, Bessa J, Peres E, Morais R, et al. Hyperspectral imaging: a review on UAV-based sensors, data processing and applications for agriculture and forestry. Remote Sens. 2017;9:1110.
[6] Xie Y, Sha Z, Yu M. Remote sensing imagery in vegetation mapping: a review. J Plant Ecol. 2008;1:9–23.
[7] Wang K, Franklin SE, Guo X, Cattet M. Remote sensing of ecology, biodiversity and conservation: a review from the perspective of remote sensing specialists. Sensors. 2010;10:9647–67.
[8] Nevalainen O, Honkavaara E, Tuominen S, Viljanen N, Hakala T, Yu X, et al. Individual tree detection and classification with UAV-based photogrammetric point clouds and hyperspectral imaging. Remote Sens. 2017;9:185.
[9] Datt B, McVicar TR, Van Niel TG, Jupp DL, Pearlman JS. Preprocessing EO-1 Hyperion hyperspectral data to support the application of agricultural indexes. IEEE Trans Geosci Remote Sens. 2003;41:1246–59.
[10] Carlson KM, Asner GP, Hughes RF, Ostertag R, Martin RE. Hyperspectral remote sensing of canopy biodiversity in Hawaiian lowland rainforests. Ecosystems. 2007;10:536–49.
[11] Elhag M, Gitas I, Othman A, Bahrawi J, Gikas P. Assessment of water quality parameters using temporal remote sensing spectral reflectance in arid environments, Saudi Arabia. Water. 2019;11:556.
[12] Frankel OH, Brown AH, Burdon JJ. The conservation of plant biodiversity. Cambridge: Cambridge University Press; 1995.
[13] Al-Rowaily SL, El-Bana MI, Al-Dujain FA. Changes in vegetation composition and diversity in relation to morphometry, soil and grazing on a hyper-arid watershed in the central Saudi Arabia. Catena. 2012;97:41–9.
[14] Hegazy A, Lovett-Doust J, Hammouda O, Gomaa N. Vegetation distribution along the altitudinal gradient in the northwestern Red Sea region. Community Ecol. 2007;8:151–62.
[15] Thenkabail PS, Lyon JG. Hyperspectral remote sensing of vegetation. Boca Raton, FL: CRC press; 2016.
[16] Swatantran A, Dubayah R, Roberts D, Hofton M, Blair JB. Mapping biomass and stress in the Sierra Nevada using lidar and hyperspectral data fusion. Remote Sens Environ. 2011;115:2917–30.
[17] Atzberger C. Advances in remote sensing of agriculture: context description, existing operational monitoring systems and major information needs. Remote Sens. 2013;5:949–81.
[18] Middleton EM, Ungar SG, Mandl DJ, Ong L, Frye SW, Campbell PE, et al. The earth observing one (EO-1) satellite mission: over a decade in space. IEEE J Sel Top Appl Earth Obs Remote Sens. 2013;6:243–56.
[19] Schlemmer M, Gitelson A, Schepers J, Ferguson R, Peng Y, Shanahan J, et al. Remote estimation of nitrogen and chlorophyll contents in maize at leaf and canopy levels. Int J Appl Earth Obs Geoinf. 2013;25:47–54.
[20] Zhang C, Kovacs JM, Wachowiak MP, Flores-Verdugo F. Relationship between hyperspectral measurements and mangrove leaf nitrogen concentrations. Remote Sens. 2013;5:891–908.

[21] Plaza A, Benediktsson JA, Boardman JW, Brazile J, Bruzzone L, Camps-Valls G, et al. Recent advances in techniques for hyperspectral image processing. Remote Sens Environ. 2009;113:S110–22.
[22] Ghamisi P, Yokoya N, Li J, Liao W, Liu S, Plaza J, et al. Advances in hyperspectral image and signal processing: a comprehensive overview of the state of the art. IEEE Geosci Remote Sens Mag. 2017;5:37–78.
[23] Burger J, Gowen A. Data handling in hyperspectral image analysis. Chemometr Intell Lab Syst. 2011;108:13–22.
[24] Su J, Yi D, Liu C, Guo L, Chen W-H. Dimension reduction aided hyperspectral image classification with a small-sized training dataset: experimental comparisons. Sensors. 2017;17:2726.
[25] Verrelst J, Romijn E, Kooistra L. Mapping vegetation density in a heterogeneous river floodplain ecosystem using pointable CHRIS/PROBA data. Remote Sens. 2012;4:2866–89.
[26] Cook B, Corp L, Nelson R, Middleton E, Morton D, McCorkel J, et al. NASA Goddard's LiDAR, hyperspectral and thermal (G-LiHT) airborne imager. Remote Sens. 2013;5:4045–66.
[27] Hook SJ, Johnson WR, Abrams MJ. NASA's hyperspectral thermal emission spectrometer (HyTES). Thermal Infrared Remote Sensing. New York: Springer; 2013. p. 93–115.
[28] Meerdink S, Roberts D, Hulley G, Gader P, Pisek J, Adamson K, et al. Plant species' spectral emissivity and temperature using the hyperspectral thermal emission spectrometer (HyTES) sensor. Remote Sens Environ. 2019;224:421–35.
[29] Vaughan RG, Calvin WM, Taranik JV. SEBASS hyperspectral thermal infrared data: surface emissivity measurement and mineral mapping. Remote Sens Environ. 2003;85:48–63.
[30] Yuan L, He Z, Lv G, Wang Y, Li C, Wang J. Optical design, laboratory test, and calibration of airborne long wave infrared imaging spectrometer. Opt Express. 2017;25:22440–54.
[31] Alfarhan A. A phytogeographical analysis of the floristic elements in Saudi Arabia. Pak J Biol Sci (Pak). 1999;2:702–11.
[32] Thomas J, Alfarhan A, Ali A, Miller A, Othman L. An account on the eastern limits of Afro-Arabian plants in South Asia. Basic Appl Dryland Res. 2008;2:12–22.
[33] El-Sheikh A, Yousef M. Halophytic and xerophytic vegetation near Al-Kharj springs. J Coll Sci Univ Riyadh. 1981;12:5.
[34] Mandaville JP, Mandaville JP. Flora of Eastern Saudi Arabia. London: Kegan Paul International; 1990.
[35] Thomas J, Basahi R, Al-Ansari AE, Sivadasan M, El-Sheikh MA, Alfarhan AH, et al. Additions to the Flora of Saudi Arabia: two new generic records from the Southern Tihama of Saudi Arabia. Natl Acad Sci Lett. 2015;38:513–6.
[36] Migahid A, Shalaby A, Batanouny K, El-Sharkawi H. Phytosociological and ecological studies of Maktila sector of Sidi-Barrani II. Ecology of the communities with 1 figure. Feddes Repert. 1975;86:83–91.
[37] Chaudhary SA. Flora of the Kingdom of Saudi Arabia, illustrated. Ministry of Agriculture & Water, National Herbarium; 1999.
[38] Batanouny KH. Plants in the deserts of the Middle East. New York: Springer Science & Business Media; 2013.
[39] Aldhebiani AY, Elhag M, Hegazy AK, Galal HK, Mufareh NS. Consideration of NDVI thematic changes in density analysis and floristic composition of Wadi Yalamlam, Saudi Arabia. Geosci Instrum Method Data Syst. 2018;7:297–306.
[40] Shaltout K, Mady M. Analysis of raudhas vegetation in central Saudi Arabia. J Arid Environ. 1996;34:441–54.
[41] Sharaf El-Din A, El-Kady H, Shaltout K, Mady M. Nutritive value of the raudhas plants in central Saudi Arabia. Arab Gulf J Sci Res. 1998;16:537–53.
[42] Hegazy A, Elhag M. Considerations of demography and life table analysis for conservation of acacia tortilis in South Sinai. World Appl Sci J. 2006;1:97–106.
[43] Al-Yemeni MN. Ecology of some plant communities in Wadi Al-Ammaria, Riyadh, Saudi Arabia. Saudi J Biol Sci. 2001;8:145–65.
[44] Taia W, El-Ghanem W. City vegetation analysis of three habitats at El-Riyadh. Bull Pure Appl Sci B. 2001;20:53–65.
[45] Hall M, Llewellyn OA, Miller AG, Al-Abbasi TM, Al-Wetaid AH, Al-Harbi RJ, et al. Important plant areas in the Arabian Peninsula: 2. Farasan archipelago. Edinb J Botany. 2010;67:189–208.
[46] Hegazy A, Doust JL. Plant ecology in the Middle East. Oxford: Oxford University Press; 2016.
[47] Niyazi B, Zaidi S, Masoud M. Comparative study of different types of digital elevation models on the basis of drainage morphometric parameters (case study of Wadi Fatimah Basin, KSA). Earth Syst Environ. 2019;3:539–50.
[48] AlNafie AH. Phytogeography of Saudi Arabia. Saudi J Biol Sci. 2008;15:159–76.
[49] Almazroui M, Ammar K, Islam MN, Awad AM, Khalid MS. Spring Saharan cyclones over Saudi Arabia: preliminary study of the impacts on climate. Earth Syst Environ. 2019;3:153–71.
[50] Juneidi M, Huss D. Rangeland resources of the Gulf and Arabian Peninsula countries and their managerial problems and needs. A preliminary survey; 1978.
[51] Tyrlis E, Lelieveld J, Steil B. The summer circulation over the eastern Mediterranean and the Middle East: influence of the South Asian monsoon. Clim Dyn. 2013;40:1103–23.
[52] Bahrawi JA, Elhag M. Simulation of sea level rise and its impacts on the western coastal area of Saudi Arabia. Indian J Geo-Marine Sci. 2016;45:54–61.
[53] Manakos I, Manevski K, Petropoulos GP, Elhag M, Kalaitzidis C. Development of a spectral library for Mediterranean land cover types. Proc 30th EARSeL Symp: remote sensing for science, education and natural and cultural heritage; 2010. p. 663–8.
[54] Manevski K, Manakos I, Petropoulos GP, Kalaitzidis C. Spectral discrimination of Mediterranean Maquis and Phrygana vegetation: results from a case study in Greece. IEEE J Sel Top Appl Earth Obs Remote Sens. 2012;5:604–16.
[55] Prasad KA, Gnanappazham L, Selvam V, Ramasubramanian R, Kar CS. Developing a spectral library of mangrove species of Indian east coast using field spectroscopy. Geocarto Int. 2015;30:580–99.
[56] Ghiringhelli LM, Carbogno C, Levchenko S, Mohamed F, Huhs G, Lüders M, et al. Towards efficient data exchange and sharing for big-data driven materials science: metadata and data formats. NPJ Comput Mater. 2017;3:1–9.
[57] Lorenz EN. Empirical orthogonal functions and statistical weather prediction. Science report 1, Statistical forecasting project, Department of Meteorology. Dep Meteorol MIT; 1956;20:130–41.
[58] Jolliffe IT, Cadima J. Principal component analysis: a review and recent developments. Philos Trans R Soc A Math Phys Eng Sci. 2016;374:20150202.
[59] Akritas MG. Bootstrapping the Kaplan–Meier estimator. J Am Stat Assoc. 1986;81:1032–8.

[60] Satten GA, Datta S. The Kaplan–Meier estimator as an inverse-probability-of-censoring weighted average. Am Statistician. 2001;55:207–10.
[61] Khan S, Naseem I, Malik MA, Togneri R, Bennamoun M. A fractional gradient descent-based rbf neural network. Circ Syst Signal Process. 2018;37:5311–32.
[62] Bassett Jr G, Koenker R. An empirical quantile function for linear models with iid errors. J Am Stat Assoc. 1982;77:407–15.
[63] Ashkar F, Ouarda TB. Approximate confidence intervals for quantiles of gamma and generalized gamma distributions. J Hydrol Eng. 1998;3:43–51.
[64] Vigneshkumar M, Yarrakula K. Comparative classification approach in hyperion imagery. Indian J Geo-Mar Sci. 2020;49(3):458–63.
[65] Elhag M, Yimaz N, Bahrawi J, Boteva S. Evaluation of optical remote sensing data in burned areas mapping of Thasos Island, Greece. Earth Syst Environ. 2020;4:813–26.
[66] Scholkmann F, Kleiser S, Metz AJ, Zimmermann R, Mata Pavia J, Wolf U, et al. A review on continuous wave functional near-infrared spectroscopy and imaging instrumentation and methodology. Neuroimage. 2014;85:6–27.
[67] Bienkowski D, Aitkenhead MJ, Lees AK, Gallagher C, Neilson R. Detection and differentiation between potato (Solanum tuberosum) diseases using calibration models trained with non-imaging spectrometry data. Comput Electron Agric. 2019;167:105056.
[68] Bolton DK. Characterizing the link between fire history, productivity, and forest structure across Canada's northern boreal using multi-source remote sensing. Vancouver, Canada: University of British Columbia; 2016.
[69] Hennessy A, Clarke K, Lewis M. Hyperspectral classification of plants: a review of waveband selection generalisability. Remote Sens. 2020;12:113.
[70] Omeer AA, Deshmukh RR. Improving the classification of invasive plant species by using continuous wavelet analysis and feature reduction techniques. Ecol Inform. 2020;61:101181.
[71] Vidhya R, Vijayasekaran D, Ramakrishnan S. Mapping invasive plant *Prosopis juliflora* in arid land using high resolution remote sensing data and biophysical parameters. Indian J Geo-Marine Sci. 2017;46:1135–44.
[72] Mureriwa N, Adam E, Sahu A, Tesfamichael S. Spectral discrimination of prosopis glandulosa (mesquite) in arid environment of South Africa: testing the utility of in situ hyperspectral data and guided regularized random forest algorithm. Manila, Philippines: Asian Association on Remote Sensing; 2015.
[73] Hoshino B, Yonemori M, Manayeva K, Karamalla A, Yoda K, Suliman M, et al. Remote sensing methods for the evaluation of the mesquite tree (*Prosopis juliflora*) environmental adaptation to semi-arid Africa. 2011 IEEE international geoscience and remote sensing symposium. IEEE; 2011. p. 1910–3.
[74] Alharthi A, El-Sheikh MA, Elhag M, Alatar AA, Abbadi GA, Abdel-Salam EM, et al. Remote sensing of 10 years changes in the vegetation cover of the northwestern coastal land of Red Sea, Saudi Arabia. Saudi J Biol Sci. 2020;27:3169–79.
[75] Suleiman I, Yaro S, Abdulwahab M, Salihu SA, Ogheneme O. Phytochemical and spectroanalytical characterizations of some plants extract as green corrosion inhibitors. J Mater Environ Sci. 2017;8:3423–32.
[76] Türker-Kaya S, Huck CW. A review of mid-infrared and near-infrared imaging: principles, concepts and applications in plant tissue analysis. Molecules. 2017;22:168.
[77] Fang F, McNeil BE, Warner TA, Maxwell AE, Dahle GA, Eutsler E, et al. Discriminating tree species at different taxonomic levels using multi-temporal WorldView-3 imagery in Washington DC, USA. Remote Sens Environ. 2020;246:111811.